ACS APPLIED MATERIALS & INTERFACES

www.acsami.org

Research Article

Multivariate Sulfonic-Based Titanium Metal−Organic Frameworks as Super-protonic Conductors

Shyamapada Nandi,[⊥] Sujing Wang,[⊥] Mohammad Wahiduzzaman,[⊥] Vibhav Yadav, Kiran Taksande, Guillaume Maurin, Christian Serre, and Sabine Devautour-Vinot*

Cite This: *ACS Appl. Mater. Interfaces* 2021, 13, 20194−20200

Read Online

ACCESS | Metrics & More | Article Recommendations | Supporting Information

ABSTRACT: The proton-conducting performances of a microporous Ti-based metal−organic framework (MOF), MIP-207, were successfully tuned using a multicomponent ligand replacement strategy to gradually introduce a controlled amount of sulfonic acid groups as a source of Brönsted acidic sites while keeping the robustness and ecofriendly synthesis conditions of the starting material. Typically, multivariate sulfonic-based solids MIP-207-$(SO_3H\text{-IPA})_x$-$(BTC)_{1-x}$ were prepared by combining various ratios of trimesate 1,3,5-benzenetricarboxylate (BTC) moieties and 5-SO_3H-isophthalate (SO_3H-IPA). The best sulfonic-MOF candidate that combines structural integrity with high proton conductivity values (*e.g.*, $\sigma = 2.6 \times 10^{-2}$ S cm^{-1} at 363 K/95% relative humidity) was further investigated using *ab initio* molecular dynamics simulations. These calculations supported that the $-SO_3H$ groups act as proton donors and revealed that the proton transfer mechanism results from the solvation structure of protons through the fast Zundel/hydronium interconversion along the continuous H-bonded network connecting the adsorbed water molecules.

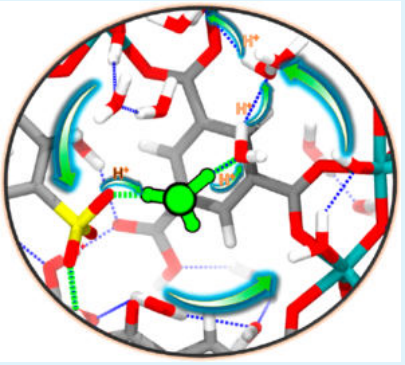

KEYWORDS: *proton conduction, multivariate metal−organic framework, Ti metal−organic framework, sulfonic-functionalized linker, proton transfer mechanism*

INTRODUCTION

Reduction in fossil fuel consumption and related greenhouse gas emissions calls for the development of clean and renewable energy systems. Fuel cells are high-potential technologies in a low-carbon future, enabling energy storage and transportation with the lowest environmental impact.[1] Several classes of fuel cells have been developed for various applications, *e.g.*, automotive, stationary, and portable power. In particular, proton-exchanged membrane fuel cells (PEMFCs) show many advantages, combining ecofriendly features with high energy conversion efficiency, high power density, and fast start-up.[2] One of the biggest bottlenecks of PEMFCs is the selection of the optimal electrolyte that permits the proton ions to pass between the electrodes while avoiding agents from mixing together. Indeed, this key component is given great attention, especially with the development of new ion-exchange membrane electrolytes combining high efficiency with durability at reduced cost. So far, the perfluorosulfonic acid polymers Nafion have been considered as a benchmark owing to their high durability, high proton conductivity at ambient conditions, good electronic insulation, very good oxidative stability, and excellent mechanical resilience.[3] However, their large-scale attractiveness is hindered because of high cost, poor dimensional stability, high fuel permeability, complex synthesis process, and above all a substantial drop of the conductivity performances at high temperature (T > 353 K). Alternative polymers[4,5] bearing sulfonic groups have been explored to replace Nafion, such as derivatives based on polyimide,[6] poly(benzimidazole),[7] aromatic poly(ether ether ketone),[8] and poly(arylene ether sulfone),[9] as well as multiblock or blend polymers.[5,10,11] Meanwhile, nanocomposite membranes using a range of fillers dispersed into the sulfonated polymer matrix have been equally investigated,[4,12] including carbon nanomaterials,[13] heteropolyacids,[14] titanium oxide,[15] zirconium oxide,[16] silica,[17,18] zeolites,[19] and ionic liquids.[20] Metal−organic frameworks (MOFs) has recently emerged in this field owing to their high structural/functional tunability, which offers multiple options to control the nature/concentration of proton sources, as well as the formation of an efficient H-bond network with the inclusion of guests as charge carriers, for an efficient proton transfer.[21−23] Inspired by the high conductivity of Nafion in relation with the hydrophilicity of its terminal sulfonic acid groups, a few MOFs containing pending $-SO_3H$ moieties grafted to the ligands were elaborated using either one-pot or postfunctional synthesis routes.[24−32] These functionalized MOFs exhibit outstanding

Received: February 24, 2021
Accepted: April 15, 2021
Published: April 22, 2021

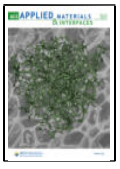

https://doi.org/10.1021/acsami.1c03644
ACS Appl. Mater. Interfaces 2021, 13, 20194−20200

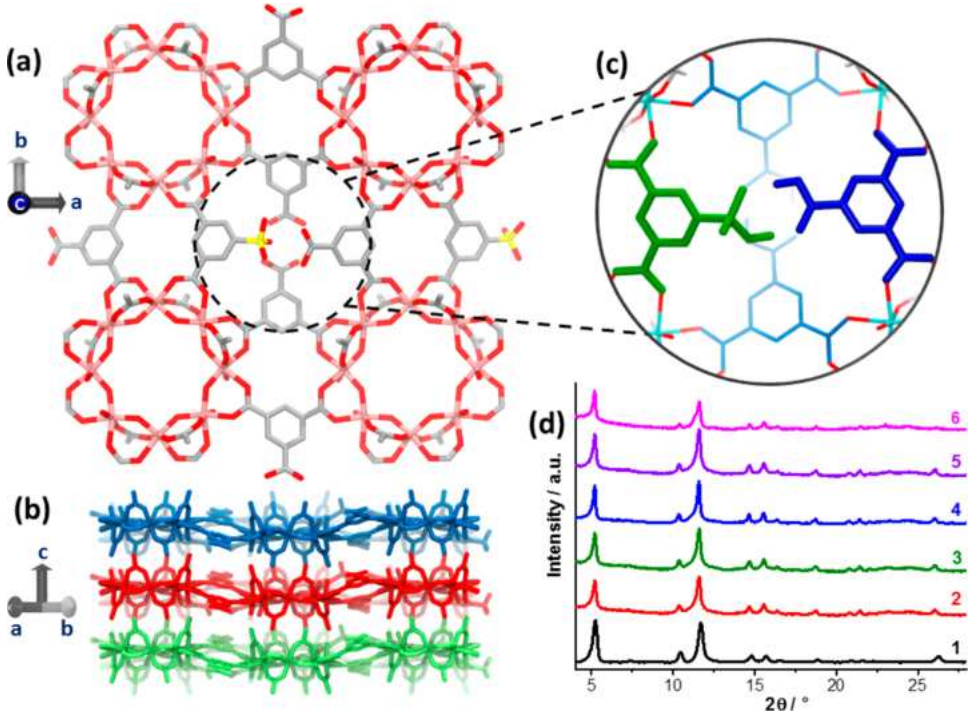

Figure 1. Illustration of the MIP-207-$(SO_3H\text{-IPA})_x(BTC)_{1-x}$ structure: (a) viewed along the *c*-axis with the atom color codes of C in gray, O in red, S in yellow, and Ti in pink; (b) 2D layered view with each layer highlighted by a distinct monocolor; (c) a zoomed view on the organization of $-SO_3H$ and $-CO_2H$ moieties, where BTC ligands and SO_3H-IPA substitutes are presented in blue and green, respectively; and (d) experimental PXRD patterns of the solid with x = 0.00 (1), 0.06 (2), 0.16 (3), 0.28 (4), 0.44 (5), and 0.66 (6).

proton conductivity, even surpassing those of Nafion in some cases.[26−31] This high-level performance results from the ability of the $-SO_3H$ groups to act as a strong H^+ donors and to initiate a continuous H-bonded network for the proton migration. Unfortunately, to date these sulfonic-based MOFs rarely combine competitive performances with good water/chemical stability and environmental friendly and scalable synthesis conditions. This clearly limits the promotion of this subclass of MOFs at the application level. To circumvent this critical issue, herein, we applied a multicomponent approach to a robust and eco-friendly 2D MOF architecture with the objective to deliberately conceive a platform of multivariate sulfonic-based solids MIP-207-$(SO_3H\text{-IPA})_x$-$(BTC)_{1-x}$, resulting from the gradual substitution of the trimesate 1,3,5-benzenetricarboxylate (BTC) moieties by 5-SO_3H-isophthalate (SO_3H-IPA) derivatives with their free sulfonic groups pointing toward the porosity. The proton donor character of the pristine sample was steadily tuned according to the mixed ligands ratio x, as illustrated by the proton conductivity rise from 8.9×10^{-5} to 2.6×10^{-2} S cm^{-1} at 363 K/95% relative humidity (RH) with x increasing from 0.00 to 0.28. Decisively, this series of MOFs remains stable under operating conditions, which further evidences that the multivariate strategy is appealing to design eco-compatible materials that fulfill the target application criteria, *i.e.*, high proton conductivity coupled to good stability under working conditions. The microscopic proton transfer mechanism in these functionalized MOFs was further elucidated using *ab initio* molecular dynamics (AIMD) simulations.

RESULTS AND DISCUSSION

The Ti-BTC MOF, where BTC refers to 1,3,5-benzenetricarboxylate moieties, also labeled as MIP-207 (MIP refers to Materials of the Institute of Porous Materials from Paris), was used as a building block for this study.[33] This material was prepared following the previously reported procedure,[33] by mixing $Ti(iPrO)_4$ with 1,3,5-benzenetricarboxylic acid in an acetic anhydride/acetic acid solution under reflux (see the Experimental Section). The resulting crystalline solid, with the chemical formula $Ti_8(\mu_2\text{-}O)_8(acetate)_8(BTC)_4$, is composed of planar octameric Ti_8 oxo-clusters, which are interconnected by BTC linkers, thus forming a two-dimensional (2D) layer (see Figure 1). The layer/layer cohesion is ensured by van der Waals interactions between acetate groups and between water/water and water/MOF under hydration conditions. The BTC organic ligand behaves somehow as an isophthalate-type linker, with the uncoordinated residual carboxylic function pointing toward the voids, so that it is able to interact with guest molecules. This ditopic bonding configuration further offers the opportunity to modify the inner surface of Ti-BTC by substituting the BTC linker with functionalized isophthalic acid (IPA) of similar molecular size and enables the formation of equivalent angles between the two connection sites. Typically, 5-SO_3H-IPA was deliberately selected to impart accessible and highly acidic proton sources to the pristine solid. We thus systematically prepared a series of mixed-ligand analogous MIP-207 solids, labeled as MIP-207-$(SO_3H\text{-IPA})_x$-$(BTC)_{1-x}$, where x ranges from 0.00 to 0.66, as confirmed by EDX and elemental analysis [see Tables S1−S6 of the Supporting Information (SI)]. According to Figure 1d, similar PXRD patterns were recorded for all MIP-207-$(SO_3H\text{-IPA})_x$-$(BTC)_{1-x}$ derivatives, evidencing that these MOFs are isostructural to the pristine MIP-207 with similar cell parameters (see Table S2, SI). This further supports that the partial replacement of the BTC linker by similar ligands in terms of dimension and topology does not impact the crystal structure of the starting material. All these samples were maintained in the incubator used for the impedance measure-

https://doi.org/10.1021/acsami.1c03644
ACS Appl. Mater. Interfaces 2021, 13, 20194−20200

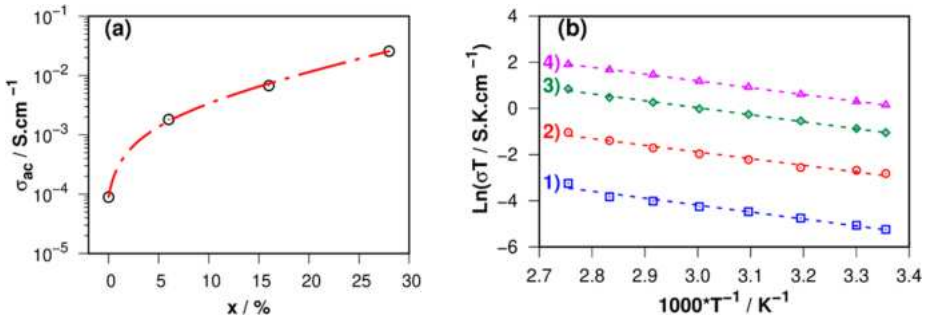

Figure 2. (a) Evolution of the conductivity (σ) for MIP-207-$(SO_3H\text{-}IPA)_x$-$(BTC)_{1-x}$ recorded at 363 K/95% RH vs the BTC substitution degree x. (b) Arrhenius-type plot of the conductivity for MIP-207-$(SO_3H\text{-}IPA)_x$-$(BTC)_{1-x}$ under 95% RH, for $x = 0$ (1), $x = 0.06$ (2), $x = 0.16$ (3), and $x = 0.28$ (4). Dashed lines correspond to the linear least-squares fit.

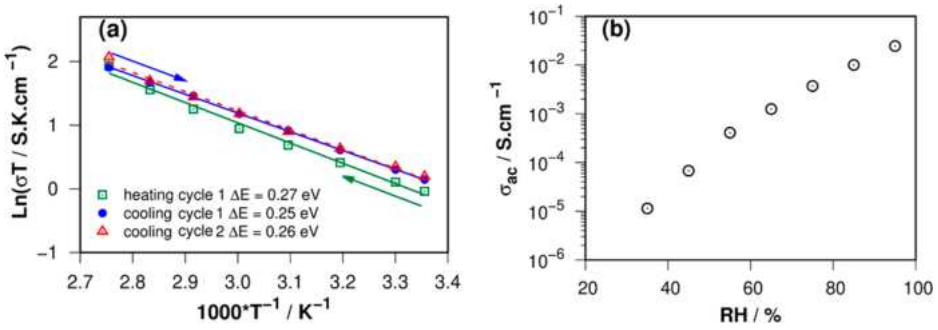

Figure 3. (a) Arrhenius-type plot of the conductivity for MIP-207-$(SO_3H\text{-}IPA)_{0.28}$-$(BTC)_{0.72}$ under 95% RH, for repeated cycles 1 and 2, under cooling (blue) and heating (red). Lines correspond to the linear least-squares fit. (b) Humidity dependence of the conductivity for MIP-207-$(SO_3H\text{-}IPA)_{0.28}$-$(BTC)_{0.72}$ recorded at 363 K.

ments at 373 K and 95% RH for 24 h, and their PXRD patterns were subsequently collected to assess their structural robustness under operating conditions. The structural integrity was maintained for all samples up to $x = 0.28$, while the materials with $x = 0.44$ and 0.66 were found to exhibit a significant loss of crystallinity (see Figure S1, SI). MIP-207-$(SO_3H\text{-}IPA)_{0.44}$-$(BTC)_{0.56}$ got semipasty, while MIP-207-$(SO_3H\text{-}IPA)_{0.66}$-$(BTC)_{0.34}$ became liquid under the humidity conditions.

Accordingly, the proton-conducting behaviors of MIP-207-$(SO_3H\text{-}IPA)_x$-$(BTC)_{1-x}$ with x up to 0.28 were further explored by ac impedance spectroscopy under varying temperature (T) and 95% RH (see Figure S3, SI). The conductivities (σ) deduced from the analysis of the Nyquist plots recorded at 363 K/95% RH are illustrated in Figure 2a and listed in Table S7 (SI). As targeted, σ gradually increases with the SO_3H-IPA amount and rises by more than 2 orders of magnitude, *i.e.*, from 8.9×10^{-5} to 2.6×10^{-2} S cm^{-1}, for x varying from 0.00 to 0.28 in MIP-207-$(SO_3H\text{-}IPA)_x$-$(BTC)_{1-x}$. This substantial increase confirms the expected benefit of grafting sulfonic functions to boost the proton conduction performance of Ti-BTC. Importantly, the excellent level of performance for MIP-207-$(SO_3H\text{-}IPA)_{0.28}$-$(BTC)_{0.72}$ makes this material among the best proton-conducting MOFs under these T/RH conditions, around 10^{-2} S cm^{-1}.[21−23]

Temperature dependence of the conductivity for MIP-207-$(SO_3H\text{-}IPA)_x$-$(BTC)_{1-x}$ was evaluated at 95% RH from the analysis of the Nyquist plots. All samples demonstrated a significant increase of conductivity with temperature according to the Arrhenius equation (Figure 2b). The corresponding activation energy is 0.25 eV for the pristine Ti-BTC, which refers to a Grotthus-like proton transfer mechanism ($\Delta E < 0.40$ eV), as regularly observed for water-mediated proton-conducting MOFs bearing free carboxylic acid functions.[21−23] Notably, ΔE does not change for the ligand-substituted derivatives, *i.e.*, neither with the pore walls' decoration with the $-SO_3H$ groups nor with the sulfonic groups' concentration. This demonstrates that the conductivity enhancement with the substitution ratio x, as illustrated in Figure 2a, results from the increase of the concentration of the strongest proton donor $-SO_3H$, while the topology of the continuous H-bonded network providing the H^+ pathway is likely unchanged.

The best material, MIP-207-$(SO_3H\text{-}IPA)_{0.28}$-$(BTC)_{0.72}$, was further explored in-depth. Figure 3a depicts the proton conductivity data collected over 24 h impedance measurements during a cooling/heating cycle at 95% RH. The deviation between the cooling and heating profiles is negligible, illustrating the reversible conductive behavior of the material with any memory effect as a prerequisite for further processing.

The role of water vapor on the conductivity performance of MIP-207-$(SO_3H\text{-}IPA)_{0.28}$-$(BTC)_{0.72}$ was characterized by recording variable-RH impedance measurements at 363 K (see Figure S4, SI). Figure 3b evidences the conductivity drop from 2.6×10^{-2} to 1.1×10^{-5} S cm^{-1} when the RH decreases from 95% to 35%. This observation strongly suggests that water contributes to the proton transfer within the material.[21−23] This statement is confirmed by the insulating behavior of MIP-207-$(SO_3H\text{-}IPA)_{0.28}$-$(BTC)_{0.72}$ at the anhydrous state, as shown by the characteristic profile of the impedance Nyquist plot recorded at 363 K, which results from an incomplete semicircle combined with high impedance values (see Figure S5, SI). This means that the H^+ long-range transfer from $-SO_3H$ donors to $-CO_2H$ or $-SO_3H$ acceptors is highly improbable in the dry state, as supported by the high activation energy for the proton conductivity ($\Delta E = 1.11$ eV, Figure S6 and Table S7, SI).

https://doi.org/10.1021/acsami.1c03644
ACS Appl. Mater. Interfaces 2021, 13, 20194−20200

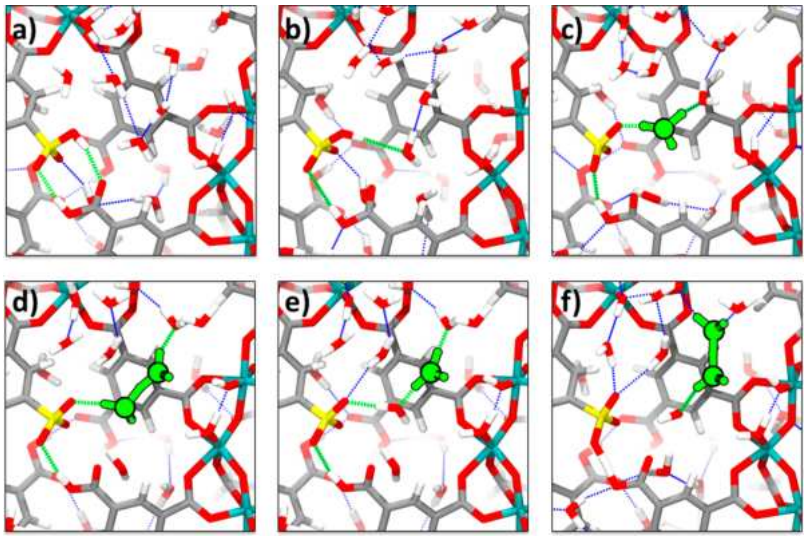

Figure 4. Illustration of the evolution of the hydrogen-bonded network and the characteristic propagation of one proton issued from the $-SO_3H$ group of the ligand and its release toward the pores of MIP-207-$(SO_3H\text{-IPA})_{0.25}$-$(BTC)_{0.75}$ as captured from the AIMD simulations performed at 400 K: (a) initial $O_{SO_3H}\cdots O_{CO_2H}$ hydrogen-bonded complex, (b) formation of a strong hydrogen bond between the proton of the $-SO_3H$ group and an adjacent adsorbed water molecule observed at 306 fs, (c) transfer of the proton to the adjacent water molecule and creation of a hydronium ion (H_3O^+) observed at 402 fs, (d) formation of a Zundel species ($H_5O_2^+$) observed at 465 fs, (e) interconversion of a Zundel species to a new hydronium ion observed at 490 fs, and (f) subsequent formation of Zundel species with the neighboring water molecule observed at 570 fs.

Accordingly, the introduction of guest molecules is a prerequisite to promote the proton transfer into the pores of the material. This suggests that, under RH conditions, the interconnection between SO_3H-proton donors and acceptors is ensured by the water molecules through the creation of a continuous H-bonded network. Molecular simulations were further implemented to gain insight into the microscopic mechanism describing the proton conduction performance of MIP-207-$(SO_3H\text{-IPA})_{0.28}$-$(BTC)_{0.72}$. A structure model for MIP-207-$(SO_3H\text{-IPA})_{0.25}$-$(BTC)_{0.75}$ was built considering that 25% of the BTC ligands were randomly substituted by $-(SO_3H$-IPA) and 25% of the acetates of the Ti−oxo cluster were also replaced arbitrarily by H_2O and OH moieties according to the NMR results (see the Supporting Information). This structure model was then geometry-optimized at the density functional theory (DFT) level, while the cell parameters were fixed according to the experimental PXRD data for MIP-207-$(SO_3H$-IPA)$_{0.28}$-$(BTC)_{0.72}$ (see Table S2, SI). Grand canonical Monte Carlo (GCMC) simulations further evidenced that this structure can host 60 water molecules per unit cell, in agreement with the uptake deduced from the experimental adsorption isotherm, *i.e.*, 56.7 molecules/unit cell (see Figure S7, SI). This water-loaded structure was then geometry-optimized at the DFT level and used as a starting configuration for further AIMD simulations (see the details in the Experimental Section). Analysis of the AIMD trajectory over 10 ps revealed the formation of a persistent 3D percolating hydrogen-bonded network that offers an optimal situation for the long-range transfer of the proton from the $-SO_3H$ function throughout the entire porosity of the solid, with the adsorbed water molecules acting as charge carriers. The radial distribution functions (RDFs) for the $O_w-O_{SO_3H}$ and O_w-O_w pairs (see Figure S9, SI) show a main peak at ∼2.7 and 2.9 Å, respectively, a signature of strong hydrogen bonds between the sulfonic groups and the adsorbed water molecules, as well as between the adsorbed species themselves.[34] Moreover the RDFs for the other O_w-O pairs, with O corresponding to the oxygen atoms of the $-CO_2H$ and of the terminal −OH and $-H_2O$ groups, exhibit a first peak at 2.9−3.1 Å (see Figure S9, SI). This clearly manifests that these functional groups can act as anchoring sites to ensure the formation of the percolated hydrogen bond network. An illustration of the resulting Grotthuss-like mechanism involved the proton transfer in this water-mediated proton conducting MOF is provided in Figure 4. The process starts with a disruption of the initial $(O-H)_{SO_3H}\cdots O_{CO_2H}$ hydrogen bond formed between the SO_3H and CO_2H groups facing each other, and there is a subsequent reorientation of the proton of the $-SO_3H$ group in order to form a hydrogen bond with an adjacent adsorbed water molecule (see Figure 4a,b). This proton is then transferred to the adsorbed water molecule to form a H_3O^+ species (see Figure 4c). This hydronium ion then migrates toward a second water molecule to form a Zundel species ($H_5O_2^+$), as shown Figure 4d. This $H_5O_2^+$ ion breaks apart to deliver a proton to a second water molecule, which forms a new H_3O^+ ion, as shown in Figure 4e, that further forms another Zundel species (Figure 4f) and so forth. We evidenced that the release of the acidic protons from the $-SO_3H$ groups occurs as fast as in Nafion,[35] typically after ∼400 fs, as illustrated in Figure 4. Noteworthy, the same scenario involving the $-CO_2H$ group rather than $-SO_3H$ as the proton donor was never observed over the whole AIMD trajectory. This clearly supports that the proton transfer exclusively proceeds via the $-SO_3H$ group, since this group is more acidic than the $-CO_2H$. Interestingly, brief disruptions in the extended hydrogen bond networks can happen, which however recover quickly, maintaining an ideal pathway. Notably, depending on the spatial organization of the adsorbed water molecules around the acidic protons of the $-SO_3H$ groups, we observed that the protons of some $-SO_3H$ groups show springlike shuttle movements featuring interchangeable donor−acceptor hydrogen bond configurations with the neighboring $-CO_2H$ groups (configurations b and c, as depicted in Figure S10, SI). A very similar behavior can also be observed between two $-CO_2H$ groups facing each other (see Figure S11, SI). This local motion refers to the dielectric relaxation behavior of the proton, which

https://doi.org/10.1021/acsami.1c03644
ACS Appl. Mater. Interfaces 2021, 13, 20194−20200

locally switches between two equilibrium positions. Since this process does not involve any water molecule's assistance, it is likely to occur at the anhydrous state, leading to the absence of long-range proton transport, as experimentally evidenced by the incomplete semicircle profile of the Nyquist plot in Figure S5 (SI).

CONCLUSIONS

A series of proton-conducting mixed-linker MOFs was devised with proton conduction performances tuned by means of a multivariate strategy that enabled a gradual substitution of the 1,3,5-benzenetricarboxylate (BTC) ligands of the pristine Ti-based MOF (MIP-207) by SO_3H-isophtalate (SO_3H-IPA) secondary linkers as precursors. MIP-207-$(SO_3H\text{-IPA})_{0.28}$-$(BTC)_{0.72}$ was identified as the optimal candidate combining a remarkable proton conductivity, *i.e.*, $\sigma = 2.6 \times 10^{-2}$ S cm^{-1} at 363 K/95% RH, and a very good stability under operating conditions. The corresponding proton transfer mechanism was elucidated at the microscopic scale by *ab initio* molecular dynamics simulations, which demonstrated a fast proton release from $-SO_3H$ groups to the adsorbed water molecules and the subsequent formation of a percolated H-bonded network along the porosity of the MOF. This study paves the way toward the development of alternative proton conductors incorporating the optimal features to achieve performance as high as the benchmark Nafion while addressing the critical issue of stability under working conditions.

EXPERIMENTAL SECTION

Synthesis of Ti-$(SO_3H\text{-IPA})_x$-$(BTC)_{1-x}$ Derivatives. 1,3,5-Benzenetricarboxylic acid (BTC) and 5-LiSO_3–IPA, the amounts of which were adjusted for each sample according to Table S1 (SI), were mixed into a round-bottom flask (50 mL). Acetic anhydride (10 mL) was added to disperse the solid with stirring at 298 K for 5 min, followed by adding acetic acid (10 mL). The system was heated to 423 K for 24 h. After cooling down to 298 K, the reaction system was filtered to collect the crude Ti-$(SO_3H\text{-IPA})_x$-$(BTC)_{1-x}$ product. Centrifugation was applied when the sample particle was too small to do filtration. The sample was washed with boiling acetone for activation. All the chemicals were purchased from commercial sources and used without further purifications.

Powder X-ray Diffraction. The PXRD patterns of all materials solids in their pristine forms and after being maintained in the incubator used for the impedance measurements at 363 K/95% RH for 24 h were collected on a PANalytical X'Pert equipped with an X'Celerator detector and using a wavelength of λ = 1.5406 Å from a generator operating at 40 kV and 30 mA.

SEM-EDX. SEM-EDX results were recorded with an FEI Magellan 400 scanning electron microscope.

NMR. ^{1}H NMR spectra were recorded on a Bruker Avance 300 spectrometer.

Elemental Analysis. Elemental analysis (EA) was performed using a Flash EA 1112 (Thermofinnigan) apparatus. EA results, listed in Table S4 (SI), are consistent with data deduced from EDX and NMR.

Conductivity Measurements. Impedance was measured using a Solartron analytical Modulab XM MTS, over a frequency range from F = 0.01 Hz to 1 MHz under 20 mV of applied ac voltage. The temperature (298–363 K) and the relative humidity [35%–95%] were fixed using an Espec Corp. SH-221 incubator. Prior to impedance recording, the solid was equilibrated under fixed T/RH conditions for 24 h. The measurements were performed using powders introduced in a homemade sample holder, allowing the use of the "two-probe" method for the electrical measurements. The resistance value of the studied solids was deduced from the analysis of the Nyquist plot [$-Z'' = f(Z')$].

For the Nyquist plots showing a well-defined semicircle (see Figures S3–S5, SI), ZView software was applied to fit impedance data sets with equivalent circuits, assembling the bulk resistance R and the bulk nonideal capacitance CPE, while a second constant phase element CPE-2 was alternatively added to account for the electrodes if applicable.

For the very lowly resistive solids, the Nyquist plot results only in the tail end of a semicircle at high frequency, while at lower frequency a capacitive tail is observed, which prevents the use of the equivalent-fitting procedure (see Figures S3–S5, SI). In that case, the resistance was evaluated from the real-axis intercept of the Nyquist plot.

The sample conductivity value was obtained using $\sigma = {}^{l}/_{R} \times {}^{l}/_{S}$, where l and S are the sample thickness and area, respectively.

According to the Arrhenius equation $\sigma(T) = {}^{\sigma_0}/_{T} \exp[{}^{-\Delta E}/_{kT}]$, where k is the Boltzmann constant, the linear fitting of $\ln(\sigma T)$ versus $1/T$ allowed us to determine the activated energy ΔE characterizing the proton transport process.

DFT Geomentry Optimization. The pristine and fully water-loaded MIP-207-$(SO_3H\text{-IPA})_{0.25}$-$(BTC)_{0.75}$ mixed-ligand structure models were optimized using periodic DFT calculations considering the Quickstep module[36] of the CP2K program[37,38] with the Gaussian plane wave (GPW) formalism. The general gradient approximation (GGA) to the exchange–correlation functional according to Perdew–Burke–Ernzerhof (PBE)[39] was combined with Grimme's DFT-D3 semiempirical dispersion corrections.[40,41] Molecularly optimized triple-ζ plus valence polarized Gaussian-type basis sets (TZVP-MOLOPT) were applied to all atoms, the Ti metal centers excepted, for which shorter-range double-ζ plus valence polarization functions (DZVP-MOLOPT) were considered.[42] The pseudopotentials derived by Goedecker, Teter, and Hutter (GTH)[43–45] were used to describe the interactions between core electrons and valence shells of the atoms. The auxiliary plane wave basis sets were truncated at 400 Ry.

Monte Carlo Simulations. Grand canonical Monte Carlo (GCMC) calculations were performed at 363 K and 95% RH to construct a starting structure model for the fully hydrated MIP-207-$(SO_3H\text{-IPA})_{0.25}$-$(BTC)_{0.75}$. Four conventional unit cells (1 × 1 × 4) were considered for the simulation box, while the atoms were maintained fixed at their initial positions. The water/MOF interactions were described by a combination of site-to-site Lennard-Jones (LJ) contributions and Coulombic terms. The LJ parameters for the atoms in the inorganic and organic part of the framework were described using a mixed set of universal force field (UFF)[46] and DREIDING force field[47] parameters, respectively (see Table S8, SI). The TIP4P/2005 potential model[48] corresponding to a microscopic representation of four LJ sites was considered to describe the water molecules (see Table S9, SI). In this simulation, all of the hydrogen atoms of the framework interact with the adsorbate water molecules via the Coulombic potential only. Atomic partial charges of the framework were derived by applying the repeat fitting strategy for the periodic system as implemented in the CP2K code[37,38,49] (see Figure S7 and Table S8, SI). Short-range dispersion forces were truncated at a cutoff radius of 12 Å, while the interactions between unlike force field centers were treated by means of the Lorentz–Berthelot combination rule. The long-range electrostatic interactions were handled using the Ewald summation technique. Typically, 2 × 10^8 Monte Carlo steps have been used for both equilibration and production runs. These MC calculations were performed using the Complex Adsorption and Diffusion Simulation Suite (CADSS) code.[50]

***Ab Initio* Molecular Dynamics.** Born–Oppenheimer first-principles MD simulations were performed on the DFT-optimized fully water-loaded MIP-207-$(SO_3H\text{-IPA})_{0.25}$-$(BTC)_{0.75}$ structure model using the CP2K package at the same level of theory and associated settings as described above for the geometry optimization. These MD simulations were performed for 10 ps in the *NVT* ensemble with a Nosé–Hoover thermostat using a time step of 0.5 fs at 400 K.

ASSOCIATED CONTENT

Supporting Information

The Supporting Information is available free of charge at https://pubs.acs.org/doi/10.1021/acsami.1c03644.

https://doi.org/10.1021/acsami.1c03644
ACS Appl. Mater. Interfaces 2021, 13, 20194–20200

Experimental procedures, synthesis, characterization of the samples, impedance spectroscopy data, water adsorption isotherm and computational details are supplied (PDF)

AUTHOR INFORMATION

Corresponding Author

Sabine Devautour-Vinot − *ICGM, University of Montpellier, CNRS, ENSCM, 34095 Montpellier, France;* orcid.org/0000-0002-3812-7379; Email: sabine.devautour-vinot@umontpellier.fr

Authors

Shyamapada Nandi − *ICGM, University of Montpellier, CNRS, ENSCM, 34095 Montpellier, France*

Sujing Wang − *Institut des Matériaux Poreux de Paris, Ecole Normale Supérieure, ESPCI Paris, CNRS, PSL University, 75005 Paris, France; CAS Key Laboratory of Microscale Magnetic Resonance, Hefei National Laboratory for Physical Sciences at the Microscale, Suzhou Institute for Advanced Research, University of Science and Technology of China, 230026 Hefei, China;* orcid.org/0000-0003-0942-2907

Mohammad Wahiduzzaman − *ICGM, University of Montpellier, CNRS, ENSCM, 34095 Montpellier, France*

Vibhav Yadav − *ICGM, University of Montpellier, CNRS, ENSCM, 34095 Montpellier, France*

Kiran Taksande − *ICGM, University of Montpellier, CNRS, ENSCM, 34095 Montpellier, France; Government of Maharashtra's Ismail Yusuf College, Mumbai, Maharashtra 411060, India*

Guillaume Maurin − *ICGM, University of Montpellier, CNRS, ENSCM, 34095 Montpellier, France*

Christian Serre − *Institut des Matériaux Poreux de Paris, Ecole Normale Supérieure, ESPCI Paris, CNRS, PSL University, 75005 Paris, France;* orcid.org/0000-0003-3040-2564

Complete contact information is available at: https://pubs.acs.org/10.1021/acsami.1c03644

Author Contributions

⊥S.N., S.W., and M.W. contributed equally to this work. The manuscript was written through contributions of all the authors. S.W. and C.S. synthesized and characterized the compounds. S.N., V.Y., K.T., and S.D.-V. carried out the electrical measurements and analysis. M.W. and G.M. were in charge of the modeling.

Notes

The authors declare no competing financial interest.

ACKNOWLEDGMENTS

The electrical measurements were performed with the support of the Balard Plateforme d'Analyses et de Caractérisation (PAC Balard). The authors thank Amine Geneste for technical assistance. Magalie Lefeuvre is acknowledged for the elemental analysis experiments. S. Wang acknowledges support from the National Natural Science Foundation of China (22071234) and the Fundamental Research Funds for the Central Universities (WK2480000007).

REFERENCES

(1) Kirubakaran, A.; Jain, S.; Nema, R. K. A Review on Fuel Cell Technologies and Power Electronic Interface. *Renewable Sustainable Energy Rev.* **2009**, *13* (9), 2430−2440.

(2) Peighambardoust, S. J.; Rowshanzamir, S.; Amjadi, M. *Review of the Proton Exchange Membranes for Fuel Cell Applications*; Elsevier Ltd., 2010; Vol. 35. DOI: 10.1016/j.ijhydene.2010.05.017.

(3) Mauritz, K. A.; Moore, R. B. State of Understanding of Nafion. *Chem. Rev.* **2004**, *104* (10), 4535−4586.

(4) Park, C. H.; Lee, C. H.; Guiver, M. D.; Lee, Y. M. Sulfonated Hydrocarbon Membranes for Medium-Temperature and Low-Humidity Proton Exchange Membrane Fuel Cells (PEMFCs). *Prog. Polym. Sci.* **2011**, *36* (11), 1443−1498.

(5) Zhang, Y.; Li, J.; Ma, L.; Cai, W.; Cheng, H. Recent Developments on Alternative Proton Exchange Membranes: Strategies for Systematic Performance Improvement. *Energy Technol.* **2015**, *3* (7), 675−691.

(6) Woo, Y.; Oh, S. Y.; Kang, Y. S.; Jung, B. Synthesis and Characterization of Sulfonated Polyimide Membranes for Direct Methanol Fuel Cell. *J. Membr. Sci.* **2003**, *220* (1−2), 31−45.

(7) Asensio, J. A.; Sánchez, E. M.; Gómez-Romero, P. G. Proton-Conducting Membranes Based on Benzimidazole Polymers for High-Temperature PEM Fuel Cells. A Chemical Quest. *Chem. Soc. Rev.* **2010**, *39* (8), 3210−3239.

(8) Iulianelli, A.; Basile, A. Sulfonated PEEK-Based Polymers in PEMFC and DMFC Applications: A Review. *Int. J. Hydrogen Energy* **2012**, *37* (20), 15241−15255.

(9) Bae, B.; Hoshi, T.; Miyatake, K.; Watanabe, M. Sulfonated Block Poly(Arylene Ether Sulfone) Membranes for Fuel Cell Applications via Oligomeric Sulfonation. *Macromolecules* **2011**, *44* (10), 3884−3892.

(10) Kang, K.; Kim, D. Pendant Dual-Sulfonated Poly(Arylene Ether Ketone) Multi-Block Copolymer Membranes for Enhanced Proton Conductivity at Reduced Water Swelling. *J. Membr. Sci.* **2019**, *578*, 103−110.

(11) Ressam, I.; Krins, N.; Laberty-Robert, C.; Selmane, M.; Lahcini, M.; Raihane, M.; Kadib, A. El; Perrot, H.; Sel, O. Sulfonic Acid Functionalized Chitosan as a Sustainable Component for Proton Conductivity Management in PEMs. *ChemistrySelect* **2017**, *2* (8), 2503−2511.

(12) Bakangura, E.; Wu, L.; Ge, L.; Yang, Z.; Xu, T. Mixed Matrix Proton Exchange Membranes for Fuel Cells: State of the Art and Perspectives. *Prog. Polym. Sci.* **2016**, *57*, 103−152.

(13) Sahu, A. K.; Ketpang, K.; Shanmugam, S.; Kwon, O.; Lee, S.; Kim, H. Sulfonated Graphene−Nafion Composite Membranes for Polymer Electrolyte Fuel Cells Operating under Reduced Relative Humidity. *J. Phys. Chem. C* **2016**, *120* (29), 15855−15866.

(14) Kim, Y. S.; Wang, F.; Hickner, M.; Zawodzinski, T. A.; McGrath, J. E. Fabrication and Characterization of Heteropolyacid (H3PW12O40)/Directly Polymerized Sulfonated Poly(Arylene Ether Sulfone) Copolymer Composite Membranes for Higher Temperature Fuel Cell Applications. *J. Membr. Sci.* **2003**, *212* (1−2), 263−282.

(15) Ketpang, K.; Shanmugam, S.; Suwanboon, C.; Chanunpanich, N.; Lee, D. Efficient Water Management of Composite Membranes Operated in Polymer Electrolyte Membrane Fuel Cells under Low Relative Humidity. *J. Membr. Sci.* **2015**, *493*, 285−298.

(16) Pan, J.; Zhang, H.; Chen, W.; Pan, M. Nafion−Zirconia Nanocomposite Membranes Formed via in Situ Sol−Gel Process. *Int. J. Hydrogen Energy* **2010**, *35* (7), 2796−2801.

(17) Choi, Y.; Kim, Y.; Kim, H. K.; Lee, J. S. Direct Synthesis of Sulfonated Mesoporous Silica as Inorganic Fillers of Proton-Conducting Organic−Inorganic Composite Membranes. *J. Membr. Sci.* **2010**, *357* (1−2), 199−205.

(18) Ibrahim, A. C.; Devautour-Vinot, S.; Naoufal, D.; Mehdi, A. Multi-Functional Hybrid Materials for Proton Conductivity. *New J. Chem.* **2012**, *36* (5), 1218.

(19) Devrim, Y.; Albostan, A. Enhancement of PEM Fuel Cell Performance at Higher Temperatures and Lower Humidities by High Performance Membrane Electrode Assembly Based on Nafion/Zeolite Membrane. *Int. J. Hydrogen Energy* **2015**, *40* (44), 15328−15335.

(20) Zanchet, L.; da Trindade, L. G.; Bariviera, W.; Nobre Borba, K. M.; Santos, R. D. M.; Paganin, V. A.; de Oliveira, C. P.; Ticianelli, E. A.; Martini, E. M. A.; de Souza, M. O. 3-Triethylammonium Propane Sulfonate Ionic Liquids for Nafion-Based Composite Membranes for PEM Fuel Cells. *J. Mater. Sci.* **2020**, *55* (16), 6928−6941.

(21) Ramaswamy, P.; Wong, N. E.; Shimizu, G. K. H. MOFs as Proton Conductors-Challenges and Opportunities. *Chem. Soc. Rev.* **2014**, *43* (16), 5913−5932.
(22) Lim, D.-W.; Kitagawa, H. Proton Transport in Metal−Organic Frameworks. *Chem. Rev.* **2020**, *120* (16), 8416−8467.
(23) Ye, Y.; Gong, L.; Xiang, S.; Zhang, Z.; Chen, B. Metal−Organic Frameworks as a Versatile Platform for Proton Conductors. *Adv. Mater.* **2020**, *32* (21), 1907090.
(24) Phang, W. J.; Jo, H.; Lee, W. R.; Song, J. H.; Yoo, K.; Kim, B.; Hong, C. S. Superprotonic Conductivity of a UiO-66 Framework Functionalized with Sulfonic Acid Groups by Facile Postsynthetic Oxidation. *Angew. Chem., Int. Ed.* **2015**, *54* (17), 5142−5146.
(25) Zhang, G.; Fei, H. Missing Metal-Linker Connectivities in a 3-D Robust Sulfonate-Based Metal-Organic Framework for Enhanced Proton Conductivity. *Chem. Commun.* **2017**, *53* (29), 4156−4159.
(26) Li, X.-M.; Dong, L.-Z.; Li, S.-L.; Xu, G.; Liu, J.; Zhang, F.-M.; Lu, L.-S.; Lan, Y.-Q. Synergistic Conductivity Effect in a Proton Sources-Coupled Metal−Organic Framework. *ACS Energy Lett.* **2017**, *2* (10), 2313−2318.
(27) Yang, F.; Xu, G.; Dou, Y.; Wang, B.; Zhang, H.; Wu, H.; Zhou, W.; Li, J.-R. R.; Chen, B. A Flexible Metal-Organic Framework with a High Density of Sulfonic Acid Sites for Proton Conduction. *Nat. Energy* **2017**, *2* (11), 877−883.
(28) Kim, S.; Joarder, B.; Hurd, J. A.; Zhang, J.; Dawson, K. W.; Gelfand, B. S.; Wong, N. E.; Shimizu, G. K. H. H. Achieving Superprotonic Conduction in Metal-Organic Frameworks through Iterative Design Advances. *J. Am. Chem. Soc.* **2018**, *140* (3), 1077−1082.
(29) Mukhopadhyay, S.; Debgupta, J.; Singh, C.; Sarkar, R.; Basu, O.; Das, S. K. Designing UiO-66-Based Superprotonic Conductor with the Highest Metal−Organic Framework Based Proton Conductivity. *ACS Appl. Mater. Interfaces* **2019**, *11* (14), 13423−13432.
(30) Devautour-Vinot, S.; Sanil, E. S.; Geneste, A.; Ortiz, V.; Yot, P. G.; Chang, J. S.; Maurin, G. Guest-Assisted Proton Conduction in the Sulfonic Mesoporous MIL-101 MOF. *Chem. - Asian J.* **2019**, *14* (20), 3561−3565.
(31) Liu, S.-S.; Han, Z.; Yang, J.-S.; Huang, S.-Z.; Dong, X.-Y.; Zang, S.-Q. Sulfonic Groups Lined along Channels of Metal−Organic Frameworks (MOFs) for Super-Proton Conductor. *Inorg. Chem.* **2020**, *59* (1), 396−402.
(32) Szufla, M.; Roztocki, K.; Krawczuk, A.; Matoga, D. One-Step Introduction of Terminal Sulfonic Groups into a Proton-Conducting Metal-Organic Framework by Concerted Deprotonation-Metalation-Hydrolysis Reaction. *Dalt. Trans.* **2020**, *49* (29), 9953−9956.
(33) Wang, S.; Reinsch, H.; Heymans, N.; Wahiduzzaman, M.; Martineau-Corcos, C.; De Weireld, G.; Maurin, G.; Serre, C. Toward a Rational Design of Titanium Metal-Organic Frameworks. *Matter* **2020**, *2* (2), 440−450.
(34) Wahiduzzaman, M.; Wang, S.; Schnee, J.; Vimont, A.; Ortiz, V.; Yot, P. G.; Retoux, R.; Daturi, M.; Lee, J. S.; Chang, J. S.; Serre, C.; Maurin, G.; Devautour-Vinot, S. A High Proton Conductive Hydrogen-Sulfate Decorated Titanium Carboxylate Metal-Organic Framework. *ACS Sustainable Chem. Eng.* **2019**, *7* (6), 5776−5783.
(35) Sagarik, K.; Phonyiem, M.; Lao-Ngam, C.; Chaiwongwattana, S. Mechanisms of Proton Transfer in Nafion®: Elementary Reactions at the Sulfonic Acid Groups. *Phys. Chem. Chem. Phys.* **2008**, *10* (15), 2098−2112.
(36) VandeVondele, J.; Krack, M.; Mohamed, F.; Parrinello, M.; Chassaing, T.; Hutter, J. Quickstep: Fast and Accurate Density Functional Calculations Using a Mixed Gaussian and Plane Waves Approach. *Comput. Phys. Commun.* **2005**, *167* (2), 103−128.
(37) Hutter, J.; Iannuzzi, M.; Schiffmann, F.; VandeVondele, J. Cp2k: Atomistic Simulations of Condensed Matter Systems. *Wiley Interdiscip. Rev. Comput. Mol. Sci.* **2014**, *4* (1), 15−25.
(38) The CP2K developers group. *CP2K*; http://www.cp2k.org (accessed 2019-02-10).
(39) Perdew, J. P.; Burke, K.; Ernzerhof, M. Generalized Gradient Approximation Made Simple. *Phys. Rev. Lett.* **1996**, *77* (18), 3865−3868.
(40) Grimme, S.; Antony, J.; Ehrlich, S.; Krieg, H. A Consistent and Accurate Ab Initio Parametrization of Density Functional Dispersion Correction (DFT-D) for the 94 Elements H-Pu. *J. Chem. Phys.* **2010**, *132* (15), 154104.
(41) Grimme, S. Accurate Description of van Der Waals Complexes by Density Functional Theory Including Empirical Corrections. *J. Comput. Chem.* **2004**, *25* (12), 1463−1473.
(42) VandeVondele, J.; Hutter, J. Gaussian Basis Sets for Accurate Calculations on Molecular Systems in Gas and Condensed Phases. *J. Chem. Phys.* **2007**, *127* (11), 114105.
(43) Goedecker, S.; Teter, M.; Hutter, J. Separable Dual-Space Gaussian Pseudopotentials. *Phys. Rev. B: Condens. Matter Mater. Phys.* **1996**, *54* (3), 1703−1710.
(44) Krack, M. Pseudopotentials for H to Kr Optimized for Gradient-Corrected Exchange-Correlation Functionals. *Theor. Chem. Acc.* **2005**, *114* (1−3), 145−152.
(45) Hartwigsen, C.; Goedecker, S.; Hutter, J. Relativistic Separable Dual-Space Gaussian Pseudopotentials from H to Rn. *Phys. Rev. B: Condens. Matter Mater. Phys.* **1998**, *58* (7), 3641−3662.
(46) Rappe, A. K.; Casewit, C. J.; Colwell, K. S.; Goddard, W. A.; Skiff, W. M. UFF, a Full Periodic Table Force Field for Molecular Mechanics and Molecular Dynamics Simulations. *J. Am. Chem. Soc.* **1992**, *114* (25), 10024−10035.
(47) Mayo, S. L.; Olafson, B. D.; Goddard, W. A. DREIDING: A Generic Force Field for Molecular Simulations. *J. Phys. Chem.* **1990**, *94* (26), 8897−8909.
(48) Abascal, J. L. F.; Vega, C. A General Purpose Model for the Condensed Phases of Water: TIP4P/2005. *J. Chem. Phys.* **2005**, *123* (23), 234505.
(49) Campañá, C.; Mussard, B.; Woo, T. K. Electrostatic Potential Derived Atomic Charges for Periodic Systems Using a Modified Error Functional. *J. Chem. Theory Comput.* **2009**, *5* (10), 2866−2878.
(50) Yang, Q.; Zhong, C. Understanding Hydrogen Adsorption in Metal-Organic Frameworks with Open Metal Sites: A Computational Study. *J. Phys. Chem. B* **2006**, *110* (2), 655−658.

https://doi.org/10.1021/acsami.1c03644
ACS Appl. Mater. Interfaces 2021, 13, 20194−20200